Chapter V

Extrapolating Beyond the Limits of Optical Microscopy: Transport Model of Bubble Growth

> Time itself must come to a stop.
> You can't get to a time before the
> big bang, because there was no
> time before the big bang.
>
> Stephen Hawking

Prof. Richard Flagan of Caltech first proposed to me the idea of estimating the nucleation time of a bubble by fitting a model and extrapolating backward in time. Prof. John Brady stressed the importance of radial convection until I found out how to account for it. Dr. Valeriy Ginzburg and Dr. Irfan Khan of Dow, Inc. offered helpful feedback on the early drafts of the model presented in this Chapter.

Time marches forward—the opportunity to observe is lost forever. The opportunity to imagine, however, is always at hand. In our imagination, we can travel to any time we wish, future, past, or present. How much can we trust our imagination to illuminate the unseen? This is the question that challenges each scientific model; by repeated agreement between the newly seen and previously imagined, the imagined models gain our trust.

Likewise, this question challenges our ability to draw any conclusions about bubble nucleation from the method proposed in Chapter III. While we hope that X-ray or light scattering might someday permit nanoscopic bubble nuclei to be detected in the present apparatus, the optical microscopy used for the present work could not detect bubbles smaller than 1 μm, two orders of magnitude larger than a bubble nucleus based on the predictions of our nucleation model (Chapter VI). This challenge is depicted in Figure V.1, but so is our solution. Using image processing, we can measure the size of bubbles with high precision over the range of 1–10 μm. As Stephen Hawking traced the expansion of the universe back to the Big Bang based on a model fit to measurements of later growth, so do we hope to trace the growth of the bubbles we observe back to their nucleation—their "Little Bang," if you will—using a model of bubble growth fit to our measurements of their later growth.

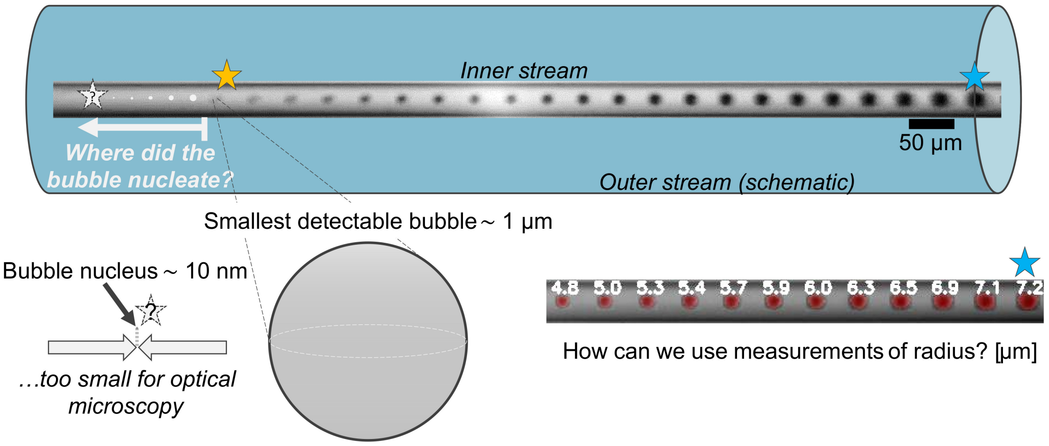

Figure V.1: Schematic of the limitations of optical microscopy in detecting bubble nucleation. Top: superposed images of the growth of a bubble from first detection inside the inner stream of polyol and CO_2 within a schematic of the outer stream (blue cylinder). The bubble was detected in an inner stream of 1k3f polyol (see Table II.1) saturated with CO_2 at 70 bar (7 MPa, 1015 psi) flowing at 50 μL/min inside a sheath of 1k5f polyol flowing at 230 μL/min inside a quartz capillary with an inner diameter of 300 μm and a length of 100 mm at 67 mm from the inlet under a 10x objective (see Table III.1). At the left side of the image of the inner stream, white dots of decreasing size indicate hypothetical bubble sizes too small to detect with optical microscopy, leading back to a hypothetical moment of bubble nucleation (star with "?"). Lower left: The size of the expected bubble nucleus of about 10 nm is shown relative to the size of the smallest bubble detectable with optical microscopy of 1 μm (bubbles are shown to the same relative scale). Lower right: segment of the same image of superposed bubble detections from the top but with image segmentation from the image-processing algorithm highlighted in red to show the quality of measurement and the estimated bubble radius in μm written in white above each bubble detection. The blue star at the right marks the same bubble observation as is marked by the blue star in the top image.

Here, we first explore the dominant physics driving bubble growth to motivate our decision to model it with the classic Epstein–Plesset model [1] in Section V.1. We consider several modifications to the original form of the model in Section V.2 and discuss how we fit these models to the data in Section V.3. The model that fits the data best assumes a diffusive flux as much as an order of magnitude larger than predicted based on the measured transport properties. We suggest that convection along the surface of the bubble steepens the concentration gradient at the surface to account for this enhanced flux and propose possible causes of this convection in Section V.3. In Section V.4, we estimate the time of nucleation during a bubble's journey along the observation capillary by fitting the visible portion of its spherical growth (1–10 μm) to a model of bubble growth and extrapolating backward in time to the critical radius of nucleation. Finally, we close with recommendations for future work in Section V.5.

V.1 Models of Bubble Growth in Supersaturated Liquids

The growth of a bubble in a supersaturated liquid is governed by several coupled effects. In general, the primary driving force for growth is considered to be the diffusion of dissolved gas from the supersaturated liquid into the bubble. This problem was solved by Epstein and Plesset for the case of a single bubble in an infinite bath of incompressible liquid held at constant temperature and pressure with a uniform diffusivity constant and fixed interfacial tension [1]. The Epstein–Plesset model neglects the effect of radial convection, which was not incorporated until the work of Scriven, who noted the similarity of this problem to the growth of a bubble in a superheated liquid [2]. Scriven also noted that many of the other factors at play in bubble growth, such as viscous resistance, inertia, and interfacial tension become negligible early in the growth of the bubble, so he only considered the asymptotic growth of the bubble at times late enough that these factors could be safely neglected. Barlow and Langlois presented a model for bubble growth that include these factors yet decouples the diffusion from the hydrodynamics by a Lagrangian transform [3]. Due to the nonlinearity of the governing equation, however, a solution could only be obtained numerically, which they achieved by assuming that the concentration primarily varies within a thin shell much smaller than the size of the bubble, similar to the work of Plesset and Zwick on the problem of bubble growth in a superheated liquid [4]. Venerus and Yala later reported that this approximation is only valid in the case of rapid bubble growth [5]. While the growth of bubbles in a foam is limited by the finite supply of dissolved gas and competition with neighboring bubbles, first modeled using the “cell model” of Amon and Denson [6], the scope of this Chapter is limited to the growth of bubbles in isolation, however.

In the present analysis, we assume that the dominant driving forces for growth are diffusion and radial convection. We neglect the effects of inertia, viscosity, and interfacial tension. As noted by Scriven [2], these factors become negligible after a short time. Barlow and Langlois [3] estimated this time scale with the following equation,

$$\frac{\rho\gamma^2\mathcal{D}}{8p_a t} + \frac{2\eta}{p_a t} + \frac{2\sigma}{p_a\gamma\sqrt{\mathcal{D}t}} \gg 1 \tag{V.1}$$

where ρ is the density of the fluid, γ is a coefficient that scales the rate of bubble growth to incorporate the effects of radial convection caused by the advancing boundary of the bubble ($\gamma = 2\beta$ for β described in equation 46 and Figure 5 of Scriven's work [2]), p_a is the pressure in the bulk liquid, η (written as μ is the original paper) is the viscosity of the bulk liquid (assumed to be constant), σ is the interfacial tension along the bubble surface (assumed to be constant), and t is the time. The first term indicates the time scale over which inertia is important, the second indicates the time scale over which viscous resistance is important, and the third indicates the time scale over which the interfacial tension is important. Inertia and viscous resistance become negligible for larger bubbles because the bubble decelerates as it grows unless there is an additional driving force (*e.g.*, decreasing pressure or raising temperature). The decreasing effect of viscous resistance was shown by Venerus *et al.* [5]. From the work of Szekely and Fang, it can be seen that increasing the importance of inertia (quantified by the dimensionless parameter B_I in their work) does not affect the rate of growth at later times, but appears just to extend the period of slower growth at the beginning [7]. Inertia may still affect bubble growth if the bubble expands extremely rapidly or takes place in a liquid metal with significantly higher density. Viscous resistance may still affect bubble growth in highly viscous media like polymer melts or viscoelastic media [8]. Interfacial tension becomes negligible for larger bubbles because the Laplace pressure decreases with the inverse of the bubble radius, as shown by Epstein and Plesset [1].

For the present work, the time scale over which these factors are important is negligible relative to the time scale of observation (hundreds of microseconds), so we neglect these factors in estimating the growth of bubbles. A rough time scale beyond which each factor becomes negligible is estimated by setting each of the three terms individually to 1 in the scaling from Barlow and Langlois (equation V.1), with the first term corresponding to inertia, the second term to viscous resistance, and the third to interfacial tension. Because each term decreases with time, times larger than this time scale will cause the terms to decrease well below one, which is the condition for these effects to be negligible according to Barlow and Langlois. To determine the maximum value for each time scale based on the properties of the system explored in the present thesis, we select the values of each parameter from the relevant range that maximize the time scale. Those ranges are: $\rho \in [0.95, 1.01]$ g/mL between 31 °C and 60 °C (see Figure II.2), $\gamma \in [1, 100]$ (see discussion later in this Section), $\mathcal{D} \in [10^{-10}, 2 \times 10^{-9}]$ m^2/s (see Figure II.4), $p_a \in [5 \times 10^5, 10^7]$ Pa (see Figure III.2 and note that bubbles are not measured in foamed region), $\eta \in [10^{-2}, 0.3]$ Pa.s (see discussion of effect of CO$_2$ on viscosity and measurements of pure polyol viscosity for 3k2f in Figure III.S1), and $\sigma \in [0.005, 0.03]$ N/m (see Figure II.3a).

- **Inertia:**

$$t_\rho \sim \frac{\rho \gamma^2 \mathcal{D}}{8 p_a} < \frac{(1000 \text{ kg/m}^3)(100)^2(10^{-9} \text{ m}^2\text{/s})}{8(5 \times 10^5 \text{ Pa})} \sim 1 \text{ ns}$$

- **Viscous Resistance:**

$$t_\eta \sim \frac{2\eta}{p_a} < \frac{2(0.3 \text{ Pa.s})}{5 \times 10^5 \text{ Pa}} \sim 1\ \mu\text{s}$$

- **Interfacial Tension:**

$$t_\sigma \sim \left(\frac{2\sigma}{p_a \gamma \sqrt{\mathcal{D}}}\right)^2 < \left(\frac{2(0.03 \text{ N/m})}{(5 \times 10^5 \text{ Pa})(1)\sqrt{10^{-10} \text{ m}^2\text{/s}}}\right)^2 \sim 40\ \mu\text{s}$$

Therefore, even if these three effects were to completely halt bubble growth over the time period that they are relevant, a model that neglects them would result in a discrepancy from the true growth of no more than 100 μs, which would have a negligible effect on the estimate of bubble nucleation in Chapter VI.

The flow in the microfluidic flow-focusing channel used to induce bubble nucleation in the present work introduces two additional factors that affect bubble growth: decreasing pressure and depletion of CO$_2$ by diffusion into the outer stream. The decreasing pressure results from the shear stress along the inner walls of the observation capillary, which leads to a roughly linear decrease in pressure along the capillary (see Figure III.2). As the pressure in the bulk fluid decreases, so does the pressure inside the bubble, though it is elevated by the Laplace pressure. As the pressure inside the bubble decreases, the gas inside expands, accelerating bubble growth. The time scale for this process is slow unless near the end of the channel relative to the field of view in experiments (about 1 mm, which corresponds to a change in pressure of about 1 bar, as in Figure III.2). Because the inner stream is ensheathed by an outer stream of pure polyol without CO_2, CO_2 dissolved in the inner stream gradually diffuses out into the outer stream. While the residence time of the fluid is typically around 100 ms and the fluids have a high viscosity—and, thus, low diffusivity—the loss of CO_2 can be significant because of the narrow dimension of the inner stream. The depletion boundary layer along the outer edge of the inner stream will grow roughly as $\sqrt{Dt} \sim \sqrt{10^{-9}\text{ m}^2/\text{s} \times 0.1\text{ s}} \sim 10\ \mu\text{m}$. Given that the inner stream radius is typically around 25 μm (see micrographs of flow channel in Figure III.3, for example), even the concentration of CO_2 at the center of the inner stream may decrease before reaching the end of the channel. The effect of depletion of CO_2 will slow bubble growth by reducing the effective bulk concentration of CO_2.

After diffusion, the most important factor affecting bubble growth is radial convection. Radial convection plays a significant role in bubble growth in the present system due to the fast growth relative to the diffusivity in the window of observation. In their review, Plesset and Prosperetti noted that the scale for the ratio of the diffusive to the convective term in the convection–diffusion equation is $\mathcal{D}/R\dot{R}$. As can be seen in the measured bubble radii in Figure V.7 (open black circles), a typical bubble might grow from 3 μm in radius to 10 μm in radius over about 1 ms. Fitting the asymptotic growth profile of $R(t) \approx a\sqrt{t - t_{nuc}}$ to these two points gives $a \approx 3\times10^{-4}\text{m}/\sqrt{\text{s}}$. The value $R\dot{R} \approx a^2/2 \approx 5\times10^{-8}$ m^2/s, while the diffusivity is at most 2×10^{-9} m^2/s (see Figure II.4). Thus, the ratio of the diffusive to the convective term is $\mathcal{D}/R\dot{R} < 0.04$, indicating that convection is more significant than diffusion in the convection–diffusion equation. To demonstrate the importance of convection, a model was constructed that incorporates all effects except for inertia and viscous resistance given that they become negligible within 1 μs. The model incorporates material properties measured using G-ADSA for the exact polyols involved and is discussed in greater depth in the SI. The model significantly underestimates the measured bubble growth, as seen in Figure V.2.

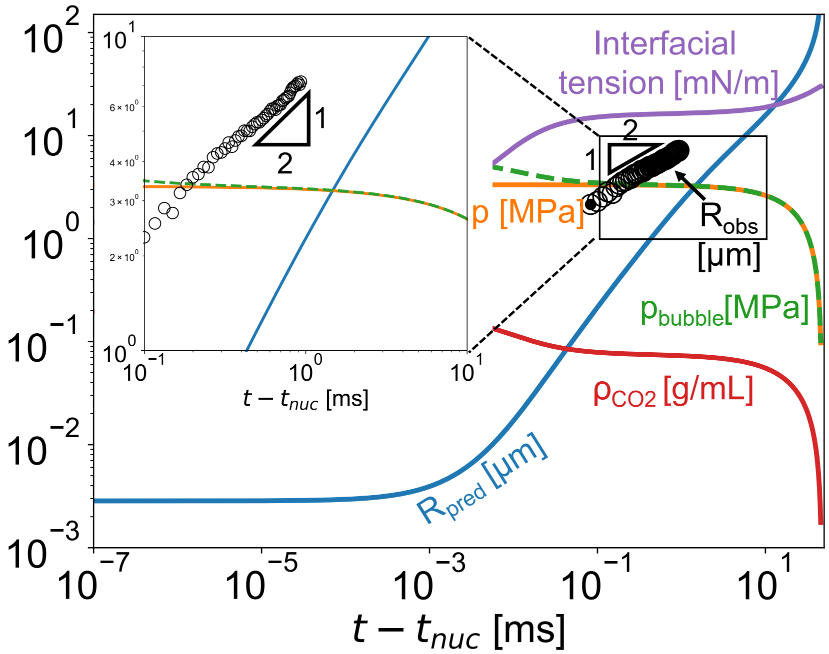

Figure V.2: Model of bubble growth excluding the effects of convection and accounting for the concentration dependence of the diffusivity plotted alongside measurements of the radius of a bubble (open black circles) over time since the estimated moment of nucleation $t - t_{nuc}$. The measurements were taken of the same bubble shown in Figure V.1. The model estimates several properties over time: the radius of the bubble R_{pred} [μm] (blue line), the density of CO_2 ρ_{CO2} [g/mL] (red line), the pressure estimated inside the channel p [MPa] (orange line), the pressure estimated inside the bubble p_{bubble} [MPa] (green dashed line), and the interfacial tension along the bubble surface [mN/m] (purple line). The inset zooms in on the region around the bubble radius measurements and highlights the underestimation of the bubble growth by the model, as well as the difference in power law behaviors (the data are matched a square root but the prediction is matched by a higher power).

Modeling the effect of radial convection explicitly can be challenging because it introduces a nonlinearity to the governing equation [3] and convection tends to introduce more numerical instability. Rather than model the effect of convection explicitly in the governing equations, we note that Scriven observed that the asymptotic solution to these equations is $R \propto \sqrt{t}$, just as in the static case modeled by Epstein and Plesset. Radial convection caused by growth in the radius of a bubble at a rate of $\dot{R}$ produces a velocity field $u = \frac{R^2}{r^2}\dot{R}$ by conservation of mass assuming spherical symmetry and an incompressible fluid. This velocity field decreases in speed with r, such that the advancing front of the bubble travels faster than the surrounding fluid. This velocity gradient causes the concentration profile of dissolved gas to be compressed into a smaller shell, increasing the concentration gradient and the flux of gas into the bubble [9]. Because the asymptotic growth is the same with or without radial convection and the asymptotic growth regime is reached before we can detect bubbles (within about 10 μs based on the time scales estimated above), we choose to model the bubble growth using the simpler static model of Epstein and Plesset and lump all the effects of convection, as well as other neglected effects, into a coefficient C by which the concentration gradient is multiplied. We will refer to this coefficient C as the "convection coefficient." This coefficient is one of several modifications made to the Epstein–Plesset model in developing the model of bubble growth used in the present work, which is discussed in the next Section.

Loss of Dissolved Gas to Pure-polymer Outer Stream Decreases Diffusion

V.2 Modified Epstein–Plesset Model Fits Measured Bubble Growth

As mentioned in the previous Section, the Epstein–Plesset model of bubble growth applies Fick's Laws to model the concentration profile of gas outside the bubble and the flux of gas into the bubble that results from the gradient, all while the surface of the bubble expands. The system and model are shown schematically in Figure V.3.

The system is assumed to be spherically symmetric, quasistatic, with no convective effects, at constant temperature and pressure, and with uniform diffusivity. In a supersaturated system, the concentration of gas in the bulk fluid c_{bulk} is greater than the concentration of gas in equilibrium with the bubble at the surface $c_{sat}(p)$. As described by Fick's First Law, this concentration gradient at the surface of the bubble causes a total flux of gas into the bubble proportional to the surface area of the bubble ($4\pi R^2$ for bubble radius R), the diffusivity of the gas in the fluid $\mathcal{D}$, and the negative concentration gradient at the surface $-\left.\frac{\partial c}{\partial r}\right|_{r=R}$. As this flux depletes CO_2 at the surface of the bubble, Fick's Second Law describes how the CO_2 in the bulk diffuses toward the depleted area. Because we have assumed that the bubble is in an infinite bath with no other bubbles around it, the boundary conditions are that the concentration at infinite radius at the unreachable end of the bath is the bulk concentration c_{bulk} and the concentration at the surface of the bubble is the equilibrium concentration $c_s(p)$. The initial condition is a uniform fluid of concentration c_{bulk}. In the case of a static boundary, Fick's Laws can be solved with a similarity variable or integral transform. Because the surface of the bubble expands as CO_2 diffuses into the bubble to maintain a constant internal density, the geometry of the concentration profile changes with time. Epstein and Plesset solved this problem—ignoring convective effects—by transforming to a simpler coordinate

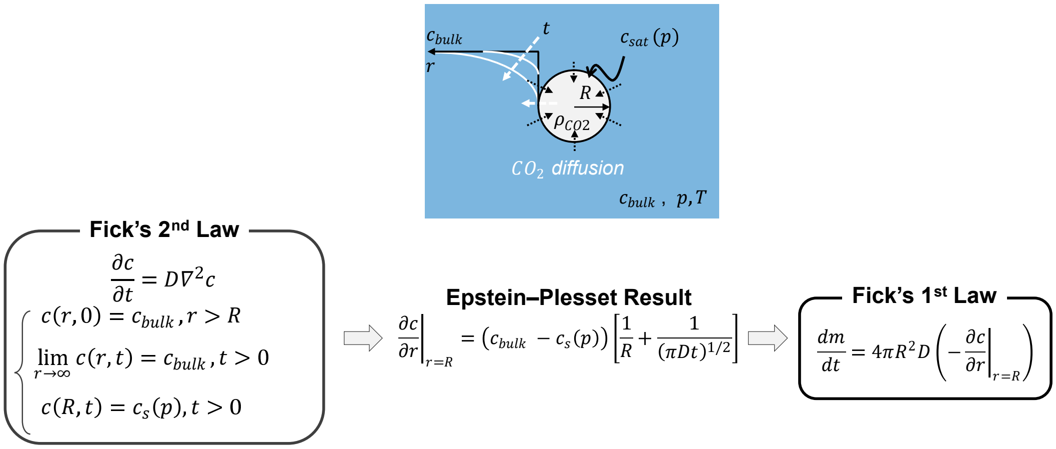

Figure V.3: Schematic showing the Epstein–Plesset model. Top: schematic of the system considered. A bubble (gray circle) with radius R and CO_2 density ρ_{CO2} is situated in an infinite fluid initially uniformly supersaturated with dissolved CO_2 (blue background) and fixed at a constant pressure p and temperature T. At the surface of the bubble, the concentration of CO_2 is fixed at the saturation pressure $c_s(p_{bub})$ for the bubble pressure p_{bub}, which is lower than the bulk concentration of CO_2 c_{bulk}. Consequently, CO_2 diffuses into the bubble (dashed black arrows), depleting CO_2 surrounding the bubble over time (white lines on the axes on the left). Bottom: flow of equations for computing bubble growth using the work of Epstein and Plesset [1]. First, Fick's Second Law (left) describes the diffusion of CO_2 outside the bubble. Next, the Epstein–Plesset result calculates the resulting concentration gradient at the surface of the bubble (middle). Finally, the flux of CO_2 into the bubble is calculated by substituting the Epstein–Plesset result into Fick's First Law (right).

system and solving for the concentration gradient at the surface of the bubble. The result is

$$\left.\frac{\partial c}{\partial r}\right|_{r=R} = (c_{bulk} - c_s(p))\left[\frac{1}{R} + \frac{1}{\sqrt{\pi \mathcal{D} t}}\right] \tag{V.2}$$

which can be substituted into Fick's First Law to determine the change in mass of gas enclosed in the bubble.

Solving for Flow and Pressure

Unlike the Epstein–Plesset system, bubbles observed in the microfluidic flow-focusing channel experience a pressure that decreases over a time scale set by the flow speed of the inner stream. Although the change in pressure during the observable growth of a bubble has a negligible effect on the size, the pressure dictates the degree of supersaturation of the mother phase, which drives the diffusion of gas into the bubble through a chemical potential gradient. We therefore must estimate the pressure at each point along the channel. Because the pressure results from the shear stress along the walls of the capillary, we must determine the properties of the flow to estimate the pressure. To determine the pressure profile and flow speed, we solved the Stokes equation for cylindrically symmetric sheath flow of two streams with different viscosities and flow rates, as shown in Figure V.4.

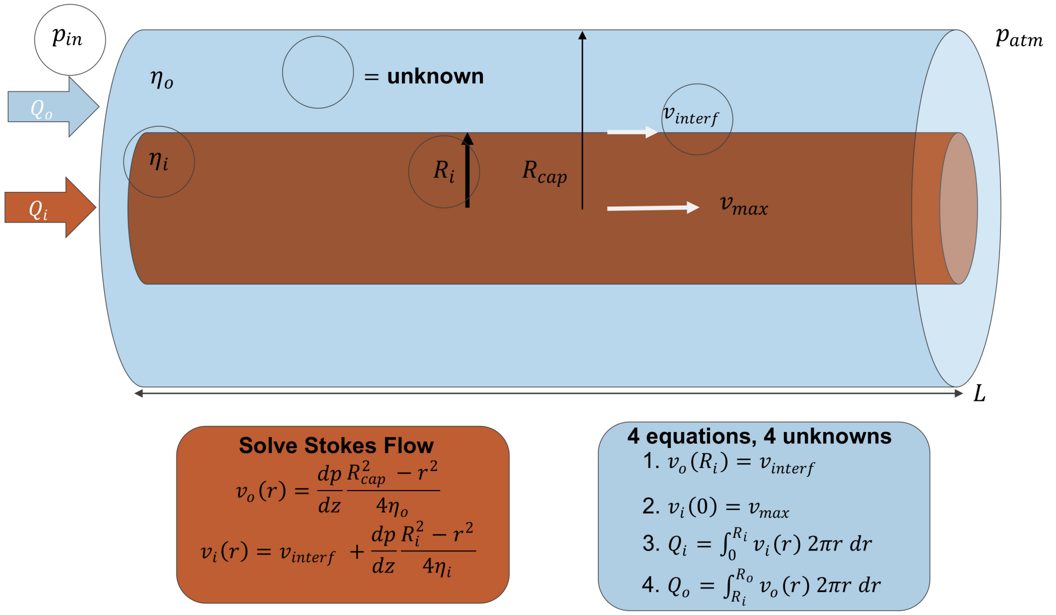

Figure V.4: Schematic showing a model of the flow in the microfluidic flow-focusing channel. Top: schematic of sheath flow with known parameters (not circled: inner stream flow rate Q_i, outer stream flow rate Q_o, outer stream viscosity η_o, inner stream center speed v_{max}, atmospheric pressure p_{atm}, inner radius of the observation capillary R_{cap}, and length of the observation capillary L) and parameters to solve for (circled: inlet pressure p_{in}, inner stream viscosity η_i, inner stream radius R_i, and speed along the interface of the inner and outer streams v_{interf}). Bottom left: axial velocity profiles as a function of radius r determined by solving pressure-driven Stokes flow in a pipe and assuming cylindrical symmetry. Bottom right: four conditions providing four equations to solve for the four unknown quantities.

We considered as known inputs the inner stream flow rate Q_i, the outer stream flow rate Q_o, the outer stream viscosity η_o, the outlet pressure p_{atm}, the length of the capillary L, the radius of the capillary R_{cap}, and the centerline speed v_{max} (since it could be measure by tracking a small bubble in a video). The inlet pressure p_{in}, the inner stream radius R_i, the velocity at the interface between the streams v_{interf}, and the inner stream viscosity η_i were unknowns to be solved for (although the inlet pressure could be compared to the pressure measured by the inner stream ISCO pump, which is close to the inlet pressure because the pressure across the low-viscosity inner stream fluid is low and the inner stream radius could be compared to rough estimates from videos, although identifying the interface precisely was challenging). These four unknowns could be solved by solving Stokes flow equations in cylindrically symmetric coordinates under pressure-driven flow along the z axis (see orange box in lower left of Figure V.4) and applying four conditions: (1) continuity of velocity at the interface $v_o(R_i) = v_i(R_i) = v_{interf}$, (2) known centerline speed $v_i(r = 0) = v_{max}$, (3) inner stream flow rate Q_i passes through cylinder of radius R_i, and (4) outer stream flow rate Q_o passes through cylindrical shell from R_i to R_{cap}.

In solving for these flow properties, we have assumed that the viscosities of the inner and outer streams are uniform throughout their respective streams. In reality, the viscosity may change by an order of magnitude or more as CO_2 diffuses into or out of a region of fluid, an estimate we base on the strong sensitivity of diffusivity on CO_2 concentration in Figure II.4 and the inverse proportionality of diffusivity and viscosity based on the Stokes–Einstein–Sutherland relationship. We have also assumed that the flow remains in steady state and that the inlet pressure is constant. In reality, we have observed that the flow may fluctuate sometimes, typically as a result of the passing of bubbles, and the inlet pressure may vary over several minutes unless the flow rate is adjusted to counteract the changes.

We validate the estimates of the inlet pressure p_{in} and inner stream radius R_i against additional measurements. While η_i is not directly measured, we can vary its value until the model solves for values of the other parameters consistent with measurements. Having measured the dimensions of the tubing from the inner stream ISCO pump to the inlet of the observation capillary, we can estimate the inlet pressure by estimating the pressure drop from the measured pressure in the ISCO pump (reported by the ISCO pump's internal pressure transducer) using the formula for pipe flow. We can do the same with the ISCO pump for the outer stream. These estimates of the inlet pressure provide a range in which the value calculated from solving the flow equations shown in Figure V.4 should lie. We can also measure a range from the inner stream radius R_i by visual observation of the recorded videos. Often, the inner stream interface is blurred due to lensing caused by the gradient in index of refraction between the inner stream of polyol and CO_2 and the outer stream of polyol. Nevertheless, bounds can be placed on the radius in which the calculated value should lie. Finally, we measure the inner stream maximum speed v_{max} by tracking small bubbles, which we assume are traveling at roughly the same speed as the flow (they do not seem to accelerate until reaching the width of the inner stream based on the data in Figure VIII.5). By measuring the speed of several bubbles, we can place a range on the input value of v_{max} as well. Because the inner stream viscosity η_i cannot be measured directly, we vary its value until the calculation for each of the measured values falls within the measured range. An example of the result of this estimation is shown in Figure V.5. At η_i = 0.01 Pa.s, the calculated values of the inner stream radius R_i, centerline velocity v, and the pressure drop across the observation capillary (Δp) are all in agreement with the measured ranges.

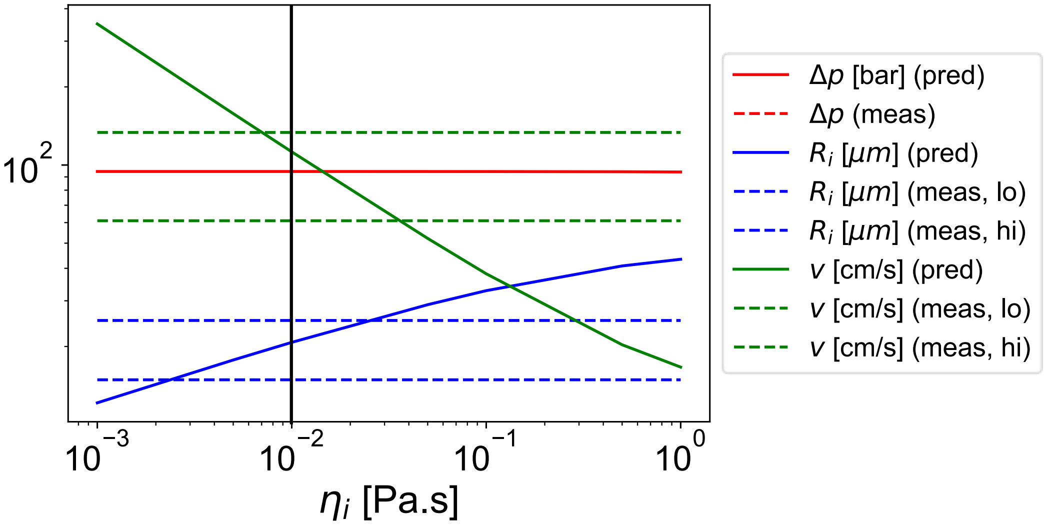

Figure V.5: Plot used to estimate the inner stream viscosity η_i [Pa.s]. Calculated values for the pressure drop across the observation capillary Δp [bar] (red), inner stream radius R_i [μm] (blue), and centerline speed v [cm/s] (green) are plotted as a function of the inner stream viscosity η_i as solid lines. Ranges of measured values are plotted as horizontal dashed lines. A value for η_i for which the calculated values are within the range of measured values is selected (0.01 Pa.s, marked by vertical black line). In this experiment, PPG 2700 g/mol saturated with CO_2 at 7.0 MPa and 22 °C was used as the inner stream.

Incorporating Material Properties

To improve the accuracy of our bubble growth model, we incorporate measured material properties of both CO_2 and polyol–CO_2 mixtures. Rather than assume that the gas inside the bubble is ideal, we determine its equation of state by interpolating pvT on CO_2 available from NIST [10]. We estimate the concentration of CO_2 at the bubble surface $c_s(p_{bubble})$, where p_{bubble} is the pressure inside the bubble, and the bulk concentration of CO_2 $c_{bulk}(p_{sat})$, where p_{sat} is the pressure at which CO_2 was saturated in the polyol–CO_2 mixture, by interpolating the solubility data measured with G-ADSA (see Figure II.6. We then estimate the interfacial tension along the surface of the bubble with the measurements from G-ADSA at different pressures (see Figure II.3a). While we measured the diffusivity of CO_2 in polyol–CO_2 mixtures at a range of pressures and temperatures (see G-ADSA measurements in Figure II.4), the Epstein–Plesset model assumes a uniform diffusivity. We explored the effect of a concentration-dependent diffusivity $\mathcal{D}(c)$ based on the measurements made with G-ADSA and report our findings in the SI. Surprisingly, we found that assuming a constant diffusivity $\mathcal{D}$ and constant convection coefficient C leads to a good fit of the measured bubble sizes, so we focused on this empirical approach instead (see next Section).

We assume that the bubble begins at a radius similar to the critical radius predicted by the model of bubble nucleation based on the string method discussed in Chapter VI, which is about 3 nm. At such small sizes, the Laplace equation $p_{bubble} = p + 2\sigma(p_{bubble})/R$ predicts enormous Laplace pressures on the order of 1 MPa. These values are unphysical, however, because the extreme curvature of nanoscopic bubbles reduces the interfacial tension because the tension is applied with a radius of curvature comparable to the molecular size. This correction to interfacial tension for small droplets was derived by Tolman and is inversely proportional to an empirical "Tolman length" [11]. We considered Tolman lengths from 5–100 nm, but found that while it provides more physical bubble pressures at the early stages of bubble growth, it does not affect the radius of the bubble by more than 1% at any point during the growth for any of the Tolman lengths considered. We selected a Tolman length of 5 nm for consistency.

Numerical Algorithm

Because the pressure inside the bubble p_{bubble} in our model depends nonlinearly on itself through the dependence of the interfacial tension in the Laplace pressure on p_{bubble} and the dependence of the radius of the bubble R on the density of CO_2 ρ_{CO2} on p_{bubble}, the modified Epstein–Plesset model in the present dissertation cannot be solved purely with finite difference methods. Instead, at each timestep, a system of self-consistent equations must be solved to determine p_{bubble} and R with a nonlinear solver (the `root` function was used from the `optimize` library of the `scipy` package [12]). A schematic of this procedure is provided in Figure V.6.

A bubble nucleus is used as the starting point for computing the bubble

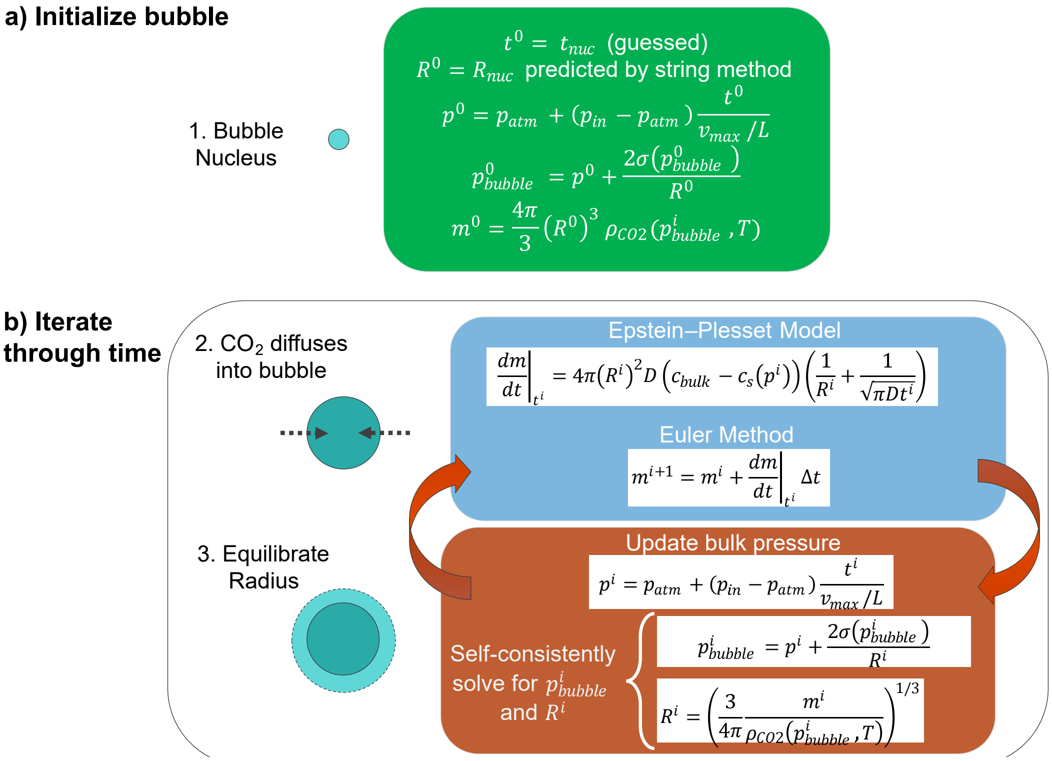

Figure V.6: Schematic of the numerical algorithm used to compute bubble growth from the modified Epstein–Plesset model. a) The bubble is initialized at a guessed nucleation time t_{nuc}, estimated radius R_{nuc}, and estimated pressure p. The pressure inside the bubble p_{bubble} is solved self-consistently and used to estimate the mass of the bubble by using the equation of state of CO_2 to estimate the density ρ_{CO2} at that pressure. b) The bubble growth is estimated by iteratively advancing in time. Each timestep consists of two parts. First, the diffusion of CO_2 into the bubble is estimated by taking an Euler timestep according to the Epstein–Plesset result for the concentration gradient at the bubble surface. Second, the bubble radius and pressure are allowed to equilibrate by self-consistently solving for their values.

growth profile with the modified Epstein–Plesset model (see Figure V.6a). The time of nucleation t_{nuc} is guessed (the algorithm for fitting t_{nuc} is described in Section V.3) and used to calculate the pressure at the corresponding location along the observation capillary using the flow parameters from the flow calculations (Figure V.4),

$$p^0 = p_{atm} + (p_{in} - p_{atm})\frac{t^0}{v_{max}/L} \tag{V.3}$$

The radius of the nucleus R_{nuc} is taken from the prediction of our nucleation model based on the string method (described in Chapter VI). Next, the pressure inside the bubble is solved self-consistently due to the dependence of the interfacial tension $\sigma(p_{bubble})$ in the Laplace pressure on the pressure in the bubble (see Figure II.3a),

$$p^0_{bubble} = p^0 + \frac{2\sigma(p^0_{bubble})}{R^0} \tag{V.4}$$

where the radius of the bubble R^0 is held fixed at R_{nuc} and the interfacial tension $\sigma(p^0_{bubble})$ is estimated by interpolating the values measured with G-ADSA (Figure II.3a). Finally, the pressure inside the bubble is used to determine the density of CO$_2$ ρ_{CO2} given the temperature T (held at laboratory temperature, $T \approx 22$ °C) and from that calculate the mass inside the bubble by multiplying by the bubble volume $\frac{4}{3}\pi(R^0)^3$.

Once the initial condition is set, the system is updated using an Euler timestep that assumes a first-order Taylor approximation of the dynamics as modeled by the Epstein–Plesset model in eq V.2 (Figure V.6b). The timestep is adapted to ensure that the discrepancy between a timestep of Δt and two timesteps of $\Delta t/2$ is below a tolerance (usually 1%). If the discrepancy is greater than the error tolerance, then the calculation for that timestep is rejected, the timestep Δt is halved, and the timestep is recalculated. If the discrepancy is smaller than the error tolerance, the calculation for that timestep is accepted and the timestep is increased by a small fraction (usually 30%). This adaptive timestep algorithm ensures that the fast dynamics at early times are calculated accurately with short timesteps while the slower dynamics at later times are calculated efficiently with larger timesteps.

Once a timestep is accepted, the properties of the bubble and the flow are updated in accordance with the increase in CO$_2$ in the bubble and the movement of the bubble down the observation capillary. The pressure is updated as in equation V.3 using the new time t^i instead of t^0. To calculate the pressure in the bubble p^i_{bubble} and the radius of the bubble R^i, the bubble pressure equation and the bubble radius equation must be solved self-consistently (step 3 in Figure V.6b), as mentioned earlier. The system is then ready to compute the next timestep. This process is repeated until the bubble reaches the end of the observation capillary, *i.e.* $t^i = L/v_{max}$.

V.3 Fitting Model to Data to Extrapolate Bubble Growth Back to Its Birth

The goal of this Chapter was to develop a model of bubble growth that could fit the observed bubble growth from about 1–10 μm in radius and extrapolate backward to the critical radius of nucleation to determine the time of nucleation. A similar technique was previously demonstrated by Leung *et al.* using the cell model of bubble growth [6] to model the growth of CO_2 bubbles in supersaturated polystyrene [13]. They explored the effects of other parameters like viscosity, interfacial tension, and the relaxation time of the polymer.

Here, the semi-empirical model used to model bubble growth has two fitted parameters: the nucleation time t_{nuc} and the "effective diffusivity" $\mathcal{D}_{eff}$. As discussed in the previous Sections, we chose to lump the effects of convection and other effects not included in the modified Epstein–Plesset model (Section V.2) into a convection coefficient C and fix the diffusivity to a constant value $\mathcal{D}$. Because both are arbitrary constants, their product is an arbitrary constant. We call their product the "effective diffusivity" $\mathcal{D}_{eff} \equiv A \times \mathcal{D}$ because although the diffusivity is unaffected by convection, convection ultimately leads to bubble growth that looks like an accelerated static diffusion problem.

Fitting Procedure for Nucleation Time

We first fit the nucleation time t_{nuc} using a bisection algorithm. We first guess a range for t_{nuc}, typically choosing the upper bound t_{nuc}^{hi} to be the time at which the bubble of interest was first observed and the lower bound as some fraction of that time (*e.g.*, 95%). We then take the average of the upper and lower bounds t_{nuc}^{lo} as our guess for t_{nuc} and calculate the bubble growth profile predicted by our modified Epstein–Plesset model (see Figure V.6).

The error between the model prediction for bubble growth and the measured bubble growth to determine if the guess for t_{nuc} should be improved. Because the effective diffusivity $\mathcal{D}_{eff}$ is not yet fit to the data, the slope of the model prediction may differ significantly from the slope of the measured bubble growth. Additionally, we want to know if the guessed nucleation time is too soon or too late. For these two reasons, we calculate the root mean *signed* squared fractional error (RMSSFE), meaning that we compute the square of the fractional error at each measurement of bubble growth and multiply by the sign of the error before taking the mean,

$$RMSSFE = \left\{ \frac{1}{N} \sum_{i=1}^{N} \mathrm{sgn}[R_{pred}(t^i) - R_{meas}(t^i)] \left[\frac{R_{pred}(t^i) - R_{meas}(t^i)}{R_{meas}(t^i)} \right]^2 \right\}^{1/2} \tag{V.5}$$

where N is the number of measurements of bubble size, $R_{meas}(t)$ is the measured bubble radius at time t, $R_{pred}(t)$ is the bubble radius predicted by the modified Epstein–Plesset model (Section V.2) at time t, and t^i is the time of the i^{th} measurement of the bubble radius. If the RMSSFE is within the tolerance (usually 0.3%), then the guessed nucleation time is accepted and the calculation proceeds to fit the effective diffusivity $\mathcal{D}_{eff}$ (see below). If the RMSSFE is not within the tolerance, the nucleation time t_{nuc} is updated. If the RMSSFE is negative, then the model underestimated the bubble growth, meaning that the nucleation time should be decreased to give the model more time to grow. The new guess for t_{nuc} is then $t_{nuc} \leftarrow (t_{nuc}^{lo} + t_{nuc})/2$ and the upper bound is updated to $t_{nuc}^{hi} \leftarrow t_{nuc}$. If the RMSSFE is positive, then the model overestimated the bubble growth, meaning that the nucleation time should be increased to reduce the time that the model grows the bubble before reaching the measurement times. The new guess for t_{nuc} is then $t_{nuc} \leftarrow (t_{nuc} + t_{nuc}^{hi})/2$ and the lower bound is updated to $t_{nuc}^{lo} \leftarrow t_{nuc}$.

Fitting Procedure for Effective Diffusivity

Once the nucleation time t_{nuc} is optimized, the effective diffusivity $\mathcal{D}_{eff}$ is optimized. As for t_{nuc}, $\mathcal{D}_{eff}$ is fit using a bisection algorithm: an upper bound $\mathcal{D}_{eff}^{hi}$ and lower bound $\mathcal{D}_{eff}^{lo}$ are selected by the user and a satisfactory fit is searched for by bisecting the interval based on the direction of the discrepancy of the model from the measurements. Because $\mathcal{D}_{eff}$ appears to affect the slope of the bubble growth on a log-log plot predicted by the model, the value is updated by comparing the slope on a log-log plot of the model to that of the measurements. Specifically, a line is fit on a log-log plot to the predicted values and another line is fit to the measured values (like a power-law fits), both at the times of measurement, and the ratio of the slope of the prediction divided by the slope of the measurement is sufficiently close to 1 (typically within 3%), the effective diffusivity $\mathcal{D}_{eff}$ is accepted along with the nucleation time t_{nuc} and the fit is complete. If the ratio is outside the tolerance from 1, the guess for $\mathcal{D}_{eff}$ is improved and the algorithm refits t_{nuc} using the new guess for $\mathcal{D}_{eff}$. If the ratio is greater than one, the effective diffusivity is too large, so it is decreased $\mathcal{D}_{eff} \leftarrow (\mathcal{D}_{eff}^{lo} + \mathcal{D}_{eff})/2$ and the upper bound is updated to $\mathcal{D}_{eff}^{hi} \leftarrow \mathcal{D}_{eff}$. If the ratio is less than one, the effective diffusivity is too small, so it is increased $\mathcal{D}_{eff} \leftarrow (\mathcal{D}_{eff} + \mathcal{D}^{hi}_{eff})/2$ and the lower bound is updated to $\mathcal{D}^{lo}_{eff} \leftarrow \mathcal{D}_{eff}$.

The resulting nucleation time t_{nuc} can be used to estimate the location of nucleation along the observation capillary d_{nuc} and, from that, the pressure at which the bubble nucleated p_{nuc}. The location of nucleation d_{nuc} is calculated by multiplying the nucleation time t_{nuc} by the centerline flow speed v_{max} to get $d_{nuc} = v_{max} t_{nuc}$. The pressure of nucleation p_{nuc} can then be computed by assuming a linear decrease in the pressure from the inlet p_{in} to atmospheric pressure p_{atm} at the outlet, $p_{nuc} = p_{in} - (p_{in} - p_{atm})\frac{d_{nuc}}{L}$. The location and pressure of nucleation will be more relevant for the discussion of bubble nucleation in Chapter VI.

Epstein–Plesset Model Fits Bubble Growth when Multiplied by Empirical Factor

Upon completion of the algorithm described above, the fitted values of the nucleation time t_{nuc} and the effective diffusivity $\mathcal{D}_{eff}$ typically yield a surprisingly accurate fit to the measured bubble radius. The accuracy is surprising given that the diffusivity, effect of convection, effect of depletion of the inner stream by diffusion of CO_2 into the outer stream, and any other effects not incorporated into the model are lumped together into a single fitted coefficient $\mathcal{D}_{eff}$. This coarse-graining is only possible because many of the factors at play (*e.g.*, viscosity, inertia) are negligible or become so at times so early as to not affect the model prediction at the relevant scales and because the effect of convection is purely a quantitative increase in the concentration gradient in the asymptotic limit. An example fit of the modified Epstein–Plesset model to the growth of bubble measured in the microfluidic flow-focusing channel with image processing is shown in Figure V.7. The uncertainty in the measurements is smaller than the marker size (open circles), yet the predicted radius R_{pred} remains well within that margin for each measurement. Note that only measurements of the bubble for sizes smaller than the inner stream are considered to reduce the effects of confinement and depletion near the edge of the inner stream. Thanks to the 60,000 fps frame rate of the high-speed camera, this restriction still left a sufficient number of points to demonstrate a good fit to the data.

An advantage of incorporating the various material properties into the modified Epstein–Plesset model, as discussed in Section V.2, is that they, too, are estimated by the model. We therefore compare their trends with those of the bubble radius over time as shown in Figure V.7. The predicted bubble radius R_{pred} begins

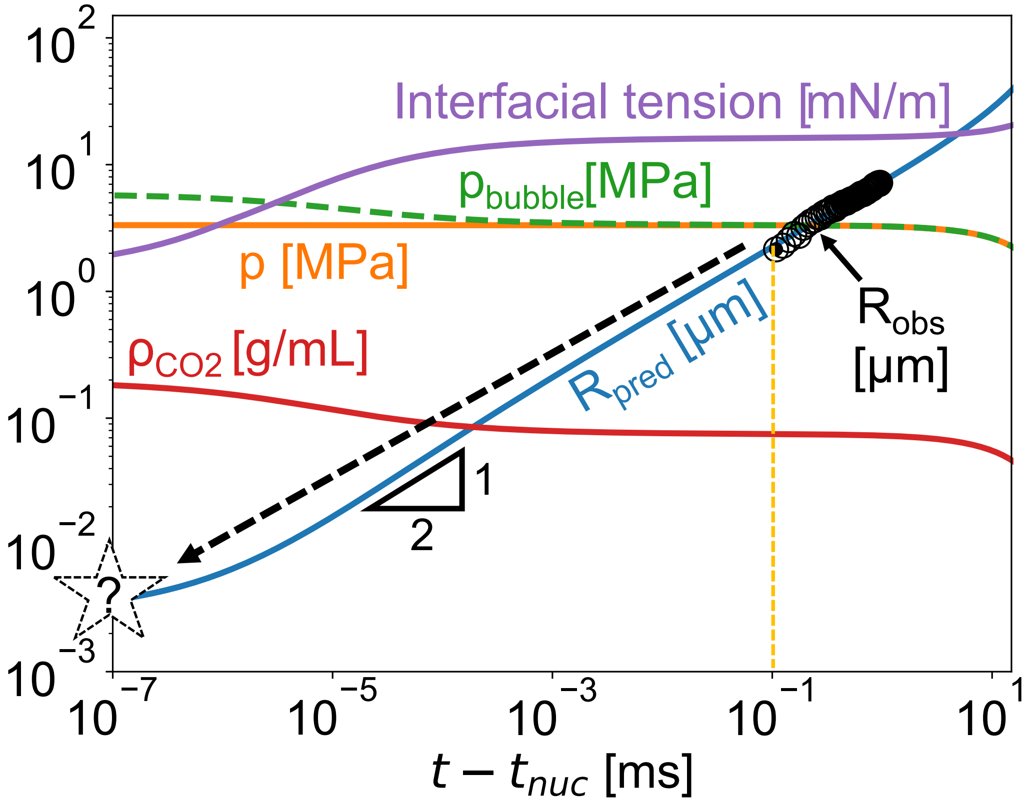

Figure V.7: Plot of the estimates of several bubble and flow properties by the modified Epstein–Plesset model fit to measured bubble radii (R_{obs} [μm], open black circles, same data as in Figure V.2) as a function of time since nucleation $t - t_{nuc}$ on a log-log plot. As in Figure V.2, the measured bubble radii grow with a 1/2 power law; the uncertainty in measurement is smaller than the marker size. The radius predicted by the model R_{pred} [μm] (blue line) passes within the uncertainty of each measurement. The moment of nucleation (star with "?") is estimated to be t_{nuc} due to the goodness of fit, which occurred about 100 μs before the first observation (marked by vertical dashed yellow line). As in Figure V.2, the interfacial tension (purple line), bubble pressure p_{bubble} (green dashed line), channel pressure p (orange line), and density of CO_2 in the bubble ρ_{CO2} (red line) are also plotted.

somewhat suppressed by interfacial tension, but quickly accelerates to the asymptotic limit of $R_{pred} \propto (t - t_{nuc})^{1/2}$ (indicated by slope triangle). At longer time scales (several milliseconds), the pressure in the bubble decreases enough that the growth accelerates beyond square-root growth, as seen by the uptick in R_{pred} at the end of the displayed trajectory. The interfacial tension is initially lower due to the Tolman correction for the effect of high curvature, then plateaus until slightly increasing as the density of CO_2 in the bubble decreases at longer time scales. The pressure in the channel decreases linearly, which appears to be slowly-then-quickly on a log-log plot. The pressure in the bubble follows the pressure in the channel once the bubble exceeds 100 nm, but at smaller sizes the effect of interfacial tension is large enough that the Laplace pressure is a significant fraction of the channel pressure. Finally, the density of CO_2 inside the bubble is at first high (0.2 g/mL) due to the high pressure in the channel and the added Laplace pressure ($2\sigma(p_{bubble})/R$) due to the small bubble radius R. It later tracks the pressure inside the bubble p_{bubble} since CO_2 is not strongly non-ideal at lower densities.

Based on this model, the bubble would have nucleated at a radius around 3 nm about 100 μs before the first observation of the bubble at about 3 μm (marked by vertical dashed yellow line). While it is likely that the neglected effects of viscous resistance and inertia further hindered the earliest, invisible bubble growth relative to the model prediction, the discrepancy is likely comparable to the time scale at which the asymptotic behavior, $R \propto (t - t_{nuc})^{1/2}$ is reached, which is around 100 ns. Such errors are negligible relative to the measurement errors (*e.g.*, the precision with which I can estimate the time for the bubble to reach the point of observation from the entrance of the observation capillary).

In this particular example, the effective diffusivity $\mathcal{D}_{eff} \approx 2.75 \times 10^{-9}$ m^2/s. This value is roughly the diffusivity of CO_2 in PPG 2700 g/mol at the saturation pressure for this experiment of 7 MPa (70 bar, 1015 psi). Nevertheless, the diffusivity near the surface of the bubble, where the pressure is at most 3.3 MPa (33 bar, 480 psi), would be less than 10^{-9} m^2/s, and we would expect that the concentration gradient would be decreased by the depletion of CO_2 into the outer stream. Such a fit could not be achieved without incorporating this enhancement of the growth through what we call the effective diffusivity $\mathcal{D}_{eff}$ and attribute largely to convective effects unless a more sophisticated model were developed. Some values for the effective diffusivity exceeded 10 times the measured diffusivity for the saturated solution, suggesting a strong effect of convection, but a correlation between flow or convective effects and the effective diffusivity has not yet been found. These values are consistent with predicted enhancement of growth based on the work of Scriven [2].

V.4 Bubble Nucleation Can Be Estimated Accurately with $R \propto (t - t_{nuc})^{1/2}$

While we learn a lot about the state of the bubble during its growth from the modified Epstein–Plesset model, it is prone to numerical errors near the condensation pressure of CO_2. Even if the pressure is not physically achieved in the bubble, it may cause sudden changes in density while solving for the pressure self-consistently when the pressure is near the condensation pressure. The model is also slow due to the need to solve for the entire growth profile for each guess of t_{nuc} and $\mathcal{D}_{eff}$, requiring hours to process the videos from a day of experiments, which amounts to a few minutes of real time recorded on high-speed video. Given that the growth quickly approaches the asymptotic behavior of $R \propto (t - t_{nuc})^{1/2}$ derived by Scriven [2], we compared the prediction of the nucleation time by fitting an asymptotic model $R(t) = a(t - t_{nuc})^{1/2}$ to the bubble growth to the prediction by the modified Epstein–Plesset model (Figure V.8). The asymptotic square-root model was fit to the data using the same bisection algorithm as used for fitting the modified Epstein–Plesset model, but because the bubble growth could be predicted by a function evaluation instead of a series of numerical timestepping and nonlinear equation-solving, the model could be fit to a day's experiments in minutes instead of hours. While the asymptotic square-root model does not provide other bubble properties like internal pressure and interfacial tension, it does model the growth as accurately as the modified Epstein–Plesset model (see Figure V.8a,b). The model fails at long times when the bubble growth is driven more by the decrease in pressure in the observation capillary, and the difference between its early predicted growth and that of the modified Epstein–Plesset model is relatively high. Nevertheless, the absolute difference between the models at early stages is small, on the order of microseconds typically. As a result, when converted to the nucleation location along the observation capillary d_{nuc} by multiplying the nucleation time t_{nuc} by the centerline flow speed v_{max} to get $d_{nuc} = v_{max} t_{nuc}$, the discrepancy in the prediction of the nucleation time between the models was below 100 μm for a population of 104 bubbles for all but one bubble, for which the discrepancy was about 1.2 mm, which is not catastrophically different (see Figure V.8c).

Because the asymptotic square-root model is faster and more stable numerically, while still agreeing closely with the predictions of nucleation time of the modified Epstein–Plesset model, we estimated the nucleation time for large populations of bubbles using the asymptotic square-root model fit. In the following Chapter, we discuss our analysis of the nucleation times and locations estimated with the bubble growth models presented in this Chapter for a large population of bubbles. In particular, we focus on the distribution of nucleation events over time and position along the observation capillary to estimate the nucleation rate at different degrees of supersaturation and demonstrate that nucleation is homogeneous.

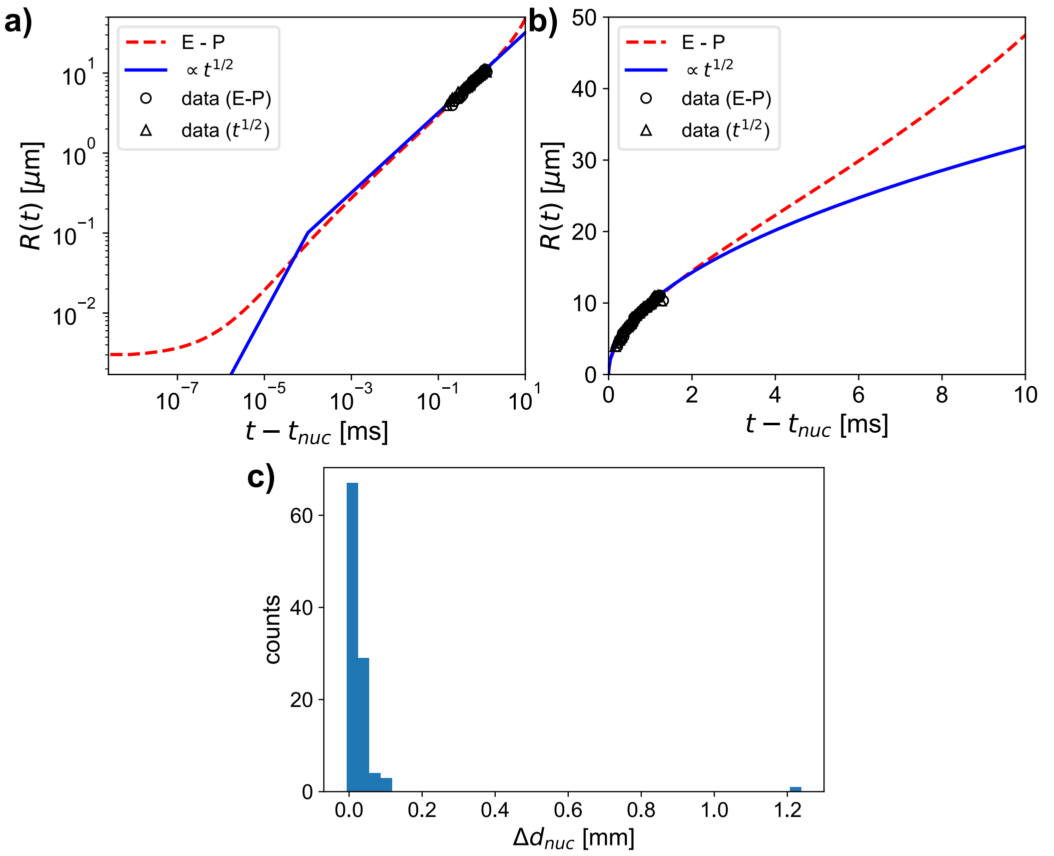

Figure V.8: a) The estimate of bubble growth using the modified Epstein–Plesset model (E - P, red dashed line) and the asymptotic square-root model ($\propto t^{1/2}$, blue line) are plotted as a function of time t since their respective estimates of the nucleation time t_{nuc}. The measured radius of a bubble observed in experiment is plotted as well. The measurements are plotted twice: once in open circles with the time measured relative to the t_{nuc} estimated with the modified Epstein–Plesset model and once in open triangles with the time measured relative to the t_{nuc} estimated with the asymptotic square-root model. The estimated values of t_{nuc} are so similar that distinguishing the two sets of markers for the measured data is difficult. b) Same as (a) but zoomed out to show the discrepancy at longer time scales due to the exclusion of pressure effects in the asymptotic square-root model. The bubble whose measured radii are plotted was observed in an inner stream of PPG 2700 g/mol and CO_2 saturated at 72 bar (7.2 MPa, 1045 psi) ensheathed in 1k5f polyol (see Table II.1) 83 mm along a 100 mm capillary with inner diameter 300 μm, at which point the pressure is estimated to be 23 bar (2.3 MPa, 335 psi). c) Histogram of the difference in the estimated nucleation location Δd_{nuc} [mm] between the two models for 104 bubbles (see Chapter VI for details on estimating the nucleation location based on the nucleation time).

V.5 Recommended Future Work

The bubble growth models presented in this Chapter provide sufficient precision in estimating the nucleation time of bubbles for us to draw conclusions about bubble nucleation in Chapter VI. Nevertheless, questions remain as to why the models we selected succeed and what underlying physics is lumped into the effective diffusivity. While we expect that the increase in the effective diffusivity relative to the true diffusivity is caused by convection, as demonstrated by Scriven [2], a study of how the addition of convection into the model affects bubble growth would be of interest. Specifically, to our knowledge, the literature lacks a clear comparison of the role of convection in accelerating bubble growth. As a suggestion, the model of Barlow and Langlois [3] could be numerically evaluated, as was done for the Epstein–Plesset model in this Chapter, but the convection term could be scaled by a dimensionless parameter $\epsilon \in [0, 1]$. A plot of the predicted bubble growth for values of ϵ in that range would provide useful insight into the extent to which convection accelerates diffusion. An extension of such a study would also solve for the concentration profile outside the bubble to test rigorously the idea that the increased bubble growth due to radial convection can be estimated by the steepening of the concentration gradient at the bubble surface. By quantitatively estimating the degree to which convection increases diffusive flux, one could elucidate the role of the other factors lumped into the effective diffusivity, such as the depletion of CO_2 or axial convection (which can also increase diffusive flux as demonstrated by the Sherwood number [14]). Another extension of such a study would explore the possibility of modeling the observed bubble growth with an Epstein–Plesset model adapted to consider a concentration-dependent diffusivity measured experimentally (*e.g.*, with G-ADSA, as in Chapter III), but scaled by a convection coefficient C. We hypothesize that the growth could be accurately modeled in this way, in which case the convection coefficient would more accurately represent the role of convection since it would be separated from the diffusivity. Such a model could also be extended to model the effect of depletion of CO_2 through diffusion into the outer stream, disentangling that factor from the effect of convection.

A study of the effect of the flow on bubble growth would also be useful in disentangling the various factors at play. We have so far assumed that the dominant form of convection is radial because the velocity gradient in the inner stream is small around small bubbles that nucleate at the center. When bubbles grow larger, or in the rare case that a bubble nucleates off-center, the bubble may no longer travel at the same speed as the surrounding fluid and, therefore, may experience nonnegligible shear convection along the surface of the bubble that might be expected to affect growth (see the work of Jae-Tack Jeong on the relative speed of a bubble in Hagen–Poiseuille flow to the surrounding fluid [15]).

Additionally, if an accurate estimate of the role of convection can be achieved, a survey of how various flow properties and bubble properties affect the role of convection would helpfully illuminate the mystery of why some bubbles have significantly higher effective diffusivities than others. While Scriven provides a formula and plot indicating the effect of different properties of the fluid on the enhancement of growth by convection, connecting that formula to measurable quantities in the experiments measuring bubble growth would extend the predictive power of Scriven's work to allow the experimentalist to estimate the role of convection under different flow or bubble conditions *a priori*.

Lastly, a convincing test of our mental model of how flow and bulk diffusion affect bubble growth would be to simulate the growth of an observed bubble with a computational fluid dynamics (CFD) simulation, such as with COMSOL or OpenFOAM. Ideally, such a model would incorporate the sheath flow profile, the radial convection caused by bubble growth, and the depletion of CO_2 from the inner stream through diffusion into the pure-polyol outer stream, as mentioned earlier, but it would also account for the effect of CO_2 concentration on the local viscosity of the fluid and the subsequent effect of viscosity variations on the flow and concentration profile in the bulk. Because measurements of the viscosity as a function of dissolved gas concentration are limited in the literature and challenging to perform due to the high pressures involved, a simple model based on the Stokes–Einstein–Sutherland relation that the viscosity $\eta \propto 1/\mathcal{D}$ could estimate viscosity as a function of the dissolved CO_2 concentration c_{CO2} using the diffusivity measurements $\mathcal{D}(c_{CO2})$ provided by G-ADSA (Figure II.4).

References

1. Epstein, P. S. & Plesset, M. S. On the Stability of Gas Bubbles in Liquid–Gas Solutions. *The Journal of Chemical Physics* **18,** 1505–1509. ISSN: 0021-9606. `http://aip.scitation.org/doi/10.1063/1.1747520` (Nov. 1950).
2. Scriven, L. On the dynamics of phase growth. *Chemical Engineering Science* **10,** 1–13. ISSN: 00092509. `https://linkinghub.elsevier.com/retrieve/pii/0009250959800191` (Apr. 1959).
3. Barlow, E. J. & Langlois, W. E. Diffusion of Gas from a Liquid into an Expanding Bubble. *IBM Journal of Research and Development* **6,** 329–337.

ISSN: 0018-8646. http://ieeexplore.ieee.org/document/5392374/ (July 1962).

4. Plesset, M. S. & Zwick, S. A. The growth of vapor bubbles in superheated liquids. *Journal of Applied Physics* **25,** 493–500. ISSN: 00218979 (1954).

5. Venerus, D. C. & Yala, N. Transport Analysis of Diffusion-Induced Bubble Growth and Collapse in Viscous Liquids. *AIChE Journal* **43,** 2948–2959. ISSN: 00011541 (1997).

6. Amon, M. & Denson, C. D. A study of the dynamics of foam growth: Analysis of the growth of closely spaced spherical bubbles. *Polymer Engineering and Science* **24,** 1026–1034. ISSN: 0032-3888. https://onlinelibrary.wiley.com/doi/10.1002/pen.760241306 (Sept. 1984).

7. Szekely, J. & Fang, S.-D. Non-equilibrium effects in the growth of spherical gas bubbles due to solute diffusionII. *Chemical Engineering Science* **28,** 2127–2140. ISSN: 00092509. https://linkinghub.elsevier.com/retrieve/pii/0009250973850031 (Dec. 1973).

8. Arefmanesh, A., Advani, S. G. & Michaelides, E. E. An accurate numerical solution for mass diffusion-induced bubble growth in viscous liquids containing limited dissolved gas. *International Journal of Heat and Mass Transfer* **35,** 1711–1722 (1992).

9. Jones, S., Evans, G. & Galvin, K. Bubble nucleation from gas cavities a review. *Advances in Colloid and Interface Science* **80,** 27–50. ISSN: 00018686. https://linkinghub.elsevier.com/retrieve/pii/S0001868698000748 (Feb. 1999).

10. NIST. *NIST Standard Reference Database Number 69* 2022. https://webbook.nist.gov/chemistry/ (2022).

11. Tolman, R. C. The Effect of Droplet Size on Surface Tension. *The Journal of Chemical Physics* **17,** 758. https://doi.org/10.1063/1.1747247 (1949).

12. Virtanen, P. *et al.* SciPy 1.0: fundamental algorithms for scientific computing in Python. *Nature Methods* **17,** 261–272. ISSN: 1548-7091. arXiv: 1907.10121. http://www.nature.com/articles/s41592-019-0686-2 (Mar. 2020).

13. Leung, S. N., Park, C. B., Xu, D., Li, H. & Fenton, R. G. Computer Simulation of Bubble-Growth Phenomena in Foaming. *Industrial & Engineering Chemistry Research* **45,** 7823–7831. ISSN: 0888-5885. https://pubs.acs.org/doi/pdf/10.1021/ie060295a%20https://pubs.acs.org/doi/10.1021/ie060295a (Nov. 2006).

14. Takemura, F. & Yabe, A. Gas dissolution process of spherical rising gas bubbles. *Chemical Engineering Science* **53,** 2691–2699. ISSN: 00092509. https://linkinghub.elsevier.com/retrieve/pii/S0009250998000943 (Aug. 1998).

15. Jeong, J. T. Axisymmetric slow viscous liquid flow around a spherical bubble translating in a circular tube. *European Journal of Mechanics, B/Fluids* **88,** 58–66. ISSN: 09977546. https://doi.org/10.1016/j.euromechflu.2021.01.001 (2021).